



Two-dimensional Inflow–Outflow Solution of Supercritical Accretion Flow

Fatemeh Zahra Zeraatgari¹, Amin Mosallanezhad², Ye-Fei Yuan², De-Fu Bu³, and Liquan Mei¹

¹ School of Mathematics and Statistics, Xi'an Jiaotong University, Xi'an, Shaanxi 710049, People's Republic of China

² Key Laboratory for Research in Galaxies and Cosmology, Department of Astronomy, University of Science and Technology of China, Hefei, Anhui 230026, People's Republic of China; mosallanezhad@ustc.edu.cn

³ Key Laboratory for Research in Galaxies and Cosmology, Shanghai Astronomical Observatory, Chinese Academy of Sciences, 80 Nandan Road, Shanghai 200030, People's Republic of China

Received 2019 October 14; revised 2019 November 4; accepted 2019 November 4; published 2020 January 10

Abstract

We present the two-dimensional inflow–outflow solutions of radiation hydrodynamic equations of supercritical accretion flows. Compared with prior studies, we include all components of the viscous stress tensor. We assume steady-state flow and use self-similar solutions in the radial direction to solve the equations in the r – θ domain of spherical coordinates. The set of differential equations have been integrated from the rotation axis to the equatorial plane. We find that the self-similarity assumption requires that the radial profile of density is described by $\rho(r) \propto r^{-0.5}$. Correspondingly, the radial profile of the mass inflow rate decreases with decreasing radius as $\dot{M}_{\text{in}} \propto r$. An inflow–outflow structure has been found in our solution. Inflow exists in the region $\theta > 65^\circ$, while above that the flow moves outward and outflow could launch. The driving forces of the outflow are analyzed and it is found that the radiation force is dominant and pushes the gas particles outward with poloidal velocity $\sim 0.25c$. The properties of the outflow are also studied. The results show that the mass flux-weighted angular momentum of the inflow is lower than that of the outflow, thus the angular momentum of the flow can be transported by the outflow. We also analyze the convective stability of the supercritical disk and find that in the absence of a magnetic field, the flow is convectively unstable. Our analytical results are fully consistent with the previous numerical simulations of supercritical accretion flow.

Unified Astronomy Thesaurus concepts: High energy astrophysics (739); Active galactic nuclei (16); Black hole physics (159); Black holes (162); Seyfert galaxies (1447)

1. Introduction

Accretion of gas through a disk onto a black hole is associated with many active phenomena in our universe such as active galactic nuclei, X-ray binaries, and extragalactic jets. Black hole accretion disks can be divided into two distinct classes based on temperature: hot and cold (see Yuan & Narayan 2014 for a review). Hot accretion flow consists of an optically thin and geometrically thick disk with very low mass accretion rate (e.g., Narayan & Yi 1994, 1995; Blandford & Begelman 1999, 2004; Yuan et al. 2012a, 2012b; Mosallanezhad et al. 2014, 2016; Zeraatgari & Abbassi 2015; Zeraatgari et al. 2018). In cold accretion flow, the disk is optically thick with a relatively high mass accretion rate.

In terms of cold accretion flow, the standard thin-disk model is the first authentic model of a black hole accretion disk (Novikov & Thorne 1973; Shakura & Sunyaev 1973; Lynden-Bell & Pringle 1974; Pringle 1981). In this model the heat generated by the viscosity locally radiates away from the disk. Consequently, the disk temperature becomes far lower than the virial temperature, i.e., 10^4 – 10^7 K. The criterion for the mass accretion rate is the Eddington rate defined as $\dot{M}_{\text{Edd}} = L_{\text{Edd}}/(\eta c^2)$, where L_{Edd} is the Eddington luminosity, η is the radiative efficiency, and c is the speed of light. The thin-disk model can successfully be applied to many black hole systems when their mass accretion rate is slightly below this, $\dot{M} \lesssim \dot{M}_{\text{Edd}}$ (e.g., Pringle 1981; Koratkar & Blaes 1999; Frank et al. 2002; Remillard & McClintock 2006; Kato et al. 2008; Abramowicz & Fragile 2013; Blaes 2014; McClintock et al. 2014).

When the accretion rate is above the Eddington limit, advection becomes important, and the accretion flow can be described by super-Eddington (or supercritical) flow. In this

case, the radiative diffusion timescale, t_{diff} , can exceed the timescale for accretion, t_{acc} , as a consequence of the high mass accretion rate. Thus, the diffused photons cannot escape from the disk and accrete onto the black hole with gas particles. Note that in some 3D radiation magnetohydrodynamic (RMHD) simulations of super-Eddington accretion (e.g., Jiang et al. 2014), it has been found that radiative transfer in the vertical direction is important, and thus photon trapping is not as strong as previously thought.

Hydrodynamic and MHD numerical simulations of hot accretion flow have found that the mass inflow rate decreases inward (e.g., Stone et al. 1999; Yuan et al. 2012b). In this regard, various analytical works proposed to explain this result by means such as an adiabatic inflow–outflow solution (ADIOS, Blandford & Begelman 1999, 2004; Begelman 2012) and convection-dominated accretion flow (CDAF, Narayan et al. 2000). In the ADIOS model, mass loss in the outflow is the reason for the inward decrease of the mass accretion rate. Therefore, due to the presence of outflow the mass accretion rate is not constant with radius and decreases toward the black hole. The CDAF model, also presented to explain the simulations, is assumed to be convectively unstable. However, recent numerical simulations have shown that MHD accretion flows are convectively stable (Narayan et al. 2012; Yuan et al. 2012a).

In the case of supercritical accretion flow, the outflow/wind is unavoidable. Since the accretion luminosity exceeds the Eddington limit, the radiation force becomes much greater than the gravity. Subsequently, at high latitudes, the gas particles can be accelerated by the radiation pressure and blown out from the system as multi-dimensional effects such as a jet/wind. Some good candidates for supercritical accretion flows are

ultraluminous X-ray sources, ultrasoft X-ray sources, narrow-line Seyfert 1 galaxies, bright microquasars (see, e.g., Wang & Zhou 1999; Boller 2000; Makishima et al. 2000; Mineshige et al. 2000; Miller et al. 2004; Done et al. 2007; Vierdayanti et al. 2010; Fürst et al. 2016; Israel et al. 2017a, 2017b; Kaaret et al. 2017; Kosec et al. 2018).

Several multi-dimensional/time-dependent radiation hydrodynamic (RHD), RMHD, and general relativistic RMHD simulations have been performed to reveal the physical properties of supercritical flows (Eggum et al. 1987, 1988; Okuda 2002; Ohsuga et al. 2005, 2009; Okuda et al. 2005; Ohsuga & Mineshige 2007, 2011; Kawashima et al. 2009, 2012; Fragile et al. 2014; Jiang et al. 2014; McKinney et al. 2014; Sadowski et al. 2014, 2015; Yang et al. 2014; Takahashi et al. 2016; Kitaki et al. 2017, 2018). The first one-dimensional analytical studies on super-Eddington accretion flow, i.e., the slim-disk model, have focused on the radial structure of the flow (Begelman & Meier 1982; Abramowicz et al. 1988; Wang & Zhou 1999; Watarai & Fukue 1999; Mineshige et al. 2000; Watarai et al. 2000, 2001; Fukue 2004; Watarai 2006; Gu & Lu 2007). They used cylindrical coordinates (R, ϕ, z) and adopted $H = c_s/\Omega_K$ for the disk height, where c_s and Ω_K are the sound speed and the Keplerian velocity, respectively. In the mentioned relation, based on hydrostatic equilibrium in the vertical direction, the disk height was considered to be constant. Although this approximation might be true for the standard thin-disk model, it is obviously inaccurate for a supercritical disk where the disk is geometrically thick due to the high mass accretion rate. However, Zeraatgari et al. (2016) solved the 1.5-dimensional inflow-outflow equations of supercritical accretion flow by assuming a power-law function for mass accretion rate, $\dot{M} \propto r^s$. They found that $s = 1$ due to the inclusion of radiative cooling. Ohsuga et al. (2005) is one of the pioneering works on numerical simulation that considered a relatively small angular momentum for the flow and obtained quasi-steady-state solutions. They found a small inflow region near the equatorial plane and a very wide-angle outflow region above the disk.

To reveal the complex two-dimensional structure and understand the physical properties of supercritical accretion flow, Gu (2012) adopted spherical polar coordinates and considered only the $T_{r\phi}$ component of the stress tensor to mimic the transfer of angular momentum by the magnetorotational instability (Balbus & Hawley 1998). He assumed that the radiation pressure is much greater than the gas pressure, i.e., $p_{\text{gas}}/p_{\text{rad}} \ll 1$. He further assumed $v_\theta = 0$, which is obviously incorrect for the extremely high mass accretion rate. By making use of radial self-similar solutions, he showed that the polytropic relation adopted in previous analytical works was not suitable. He found that even for marginally sub-Eddington accretion flow the energy advection was significant and the accretion disk was convectively stable.

In the present study, we revisit the inflow-outflow structure of supercritical accretion flow by means of a radial self-similar solution. The main aim of this study is to relax the assumption of $v_\theta = 0$ made by Gu (2012) and consider a very high mass accretion rate (see Figure 1 of Gu 2012 for more details). To do so, we adopt spherical coordinates and consider all components of the velocity, i.e., (v_r, v_θ, v_ϕ) , and also all components of the viscous stress tensor. We integrate the set of coupled RHD equations over all vertical angles, from the rotational axis to the equatorial plane. Therefore, unlike previous analytical works, we can clearly show the two-dimensional structure of the

supercritical disk and address its physical properties when the disk is in a steady state.

The remainder of the manuscript is organized as follows. The basic equations and assumptions are described in Section 2. The self-similar solutions and boundary conditions are given in Section 3. In Section 4, the numerical results are presented with detailed explanations. Finally, the summary and discussion are provided in Section 5.

2. Basic Equations and Assumptions

In this section, we describe the two-dimensional RHD equations of accretion flow around a non-rotating black hole in spherical coordinates (r, θ, ϕ) . We neglect the self-gravity of the accretion disk. To avoid relativistic effects, the Newtonian potential, $\psi = -GM/r$, is considered, where G is the gravitational constant and M is the black hole mass. The basic RHD equations of the accretion flow are written as follows:

$$\frac{\partial \rho}{\partial t} + \nabla \cdot (\rho \mathbf{v}) = 0, \quad (1)$$

$$\rho \left[\frac{\partial \mathbf{v}}{\partial t} + (\mathbf{v} \cdot \nabla) \mathbf{v} \right] = -\rho \nabla \psi - \nabla p_{\text{gas}} + \nabla \cdot \boldsymbol{\sigma} + \frac{\chi}{c} \mathbf{F}, \quad (2)$$

$$\frac{\partial e}{\partial t} + \nabla \cdot (e \mathbf{v}) = -p_{\text{gas}} \nabla \cdot \mathbf{v} - 4\pi \kappa B + c \kappa E + \Phi_{\text{vis}}, \quad (3)$$

$$\frac{\partial E}{\partial t} + \nabla \cdot (E \mathbf{v}) = -\nabla \cdot \mathbf{F} - \nabla \mathbf{v} : \mathbf{P} + 4\pi \kappa B - c \kappa E. \quad (4)$$

In the above equations, ρ is the density, $\mathbf{v} = (v_r, v_\theta, v_\phi)$ is the velocity, p_{gas} is the gas pressure, $\boldsymbol{\sigma}$ is the viscous stress tensor, χ is the total opacity, \mathbf{F} is the radiation flux, e is the internal energy density of the gas, E is the radiation energy density, \mathbf{P} is the radiation pressure tensor, κ is the absorption opacity, B is the blackbody intensity, and Φ_{vis} is the viscous dissipative function. The viscous stress tensor can be described as

$$\sigma_{ij} = \mu \left[\left(\frac{\partial v_j}{\partial x_i} + \frac{\partial v_i}{\partial x_j} \right) - \frac{2}{3} (\nabla \cdot \mathbf{v}) \delta_{ij} \right] \quad (5)$$

where $\mu \equiv \nu \rho$ is the dynamical viscosity coefficient, which determines the magnitude of the stress, and ν is called the kinematic viscosity coefficient. We note that the bulk viscosity is neglected in this study. The dynamical viscosity coefficient is calculated with the usual α prescription of the viscosity (Shakura & Sunyaev 1973),

$$\mu = \alpha \frac{p_{\text{gas}} + \lambda E}{\Omega_K}, \quad (6)$$

where α is the viscosity parameter, λ is the flux limiter, and $\Omega_K \equiv (GM/r^3)^{1/2}$ is the Keplerian angular momentum. To calculate the radiation flux, \mathbf{F} , we apply the flux-limited diffusion approximation (Levermore & Pomraning 1981) as

$$\mathbf{F} = -\frac{\lambda c}{\chi} \nabla E, \quad (7)$$

where λ is the flux limiter. To avoid complexity, the absorption opacity including both free-free absorption, κ_{ff} , and bound-free absorption, κ_{bf} , is neglected in the present study. The total opacity is then $\chi = \rho \kappa_{\text{es}}$, where κ_{es} is the electron scattering

opacity. The radiation pressure tensor is calculated in terms of the energy density of the radiation as

$$\mathbf{P} = f\mathbf{E}, \quad (8)$$

where f is the Eddington tensor. In this study we focus on the optically thick region, where $\lambda = 1/3$ and $f = \mathbf{I}/3$ (Kato et al. 2008). Thus, the Eddington approximation yields

$$P_{ij} = \begin{cases} p_{\text{rad}} = E/3 & \text{if } i = j, \\ 0 & \text{if } i \neq j. \end{cases} \quad (9)$$

By combining Equations (3) and (4), the total energy equation including gas and radiation can be rewritten as

$$\begin{aligned} \frac{\partial(e + E)}{\partial t} + \nabla \cdot [(e + E)\mathbf{v}] \\ = -(p_{\text{gas}} + p_{\text{rad}})\nabla \cdot \mathbf{v} - \nabla \cdot \mathbf{F} + \Phi_{\text{vis}}, \end{aligned} \quad (10)$$

where p_{rad} is radiation pressure, and based on our assumption it is much greater than the gas pressure, i.e., $p_{\text{gas}}/p_{\text{rad}} \ll 1$.⁴ Thus, the gas pressure as well as internal energy density of the gas will be dropped in our equations. We consider steady-state and axisymmetric ($\partial/\partial t = \partial/\partial \phi = 0$) flow to solve Equations (1)–(4). The detailed forms of the partial differential equations are presented in Appendix A (see Equations (45)–(51)). We outline our self-similar solutions and boundary conditions in the following section.

3. Self-similar Solutions and Boundary Conditions

Many numerical simulations of accretion flow show that the radial profile of the density can be described as a power-law function of r as $\rho(r) \propto r^{-n}$. In terms of hot accretion flow, the global numerical simulations are consistent with the self-similar assumptions away from the boundaries (e.g., Stone et al. 1999; Yuan et al. 2012a, 2012b, 2015). For the case of super-Eddington accretion flow, recent numerical simulations also show that the radial profile of the density follows a power-law form with $n \approx 0.55$ for a wide range of α from $\alpha = 0.005$ to 0.1 (Ohsuga et al. 2005; Yang et al. 2014).⁵ Therefore, in order to solve Equations (45)–(49) by numerical methods, we adopt self-similar solutions to remove the radial dependence of the variables.

3.1. Self-similar Solutions

By considering a fiducial radial distance, i.e., r_0 , the self-similar solutions can be written as a power-law form of r/r_0 . Thus, the physical variables of the flow can be written using the following radial scaling:

$$v_r(r, \theta) = v_0 \left(\frac{r}{r_0} \right)^{-1/2} v_r(\theta), \quad (11)$$

$$v_\theta(r, \theta) = v_0 \left(\frac{r}{r_0} \right)^{-1/2} v_\theta(\theta), \quad (12)$$

$$v_\phi(r, \theta) = v_0 \left(\frac{r}{r_0} \right)^{-1/2} \Omega(\theta) \sin \theta, \quad (13)$$

$$\rho(r, \theta) = \rho_0 \left(\frac{r}{r_0} \right)^{-n} \rho(\theta), \quad (14)$$

$$p_{\text{rad}}(r, \theta) = \rho_0 v_0^2 \left(\frac{r}{r_0} \right)^{-n-1} p(\theta), \quad (15)$$

where $v_0 = (GM/r_0)^{1/2}$ and ρ_0 are considered to be the Keplerian velocity and density at r_0 , respectively. By substituting the above self-similar solutions into Equations (45)–(49), the radial dependence will be removed only if $n = 1/2$. This is mainly due to the inclusion of the radiative cooling in the energy equation, i.e., $\nabla \cdot \mathbf{F}$. Consequently, the radial profile of the accretion rate can be well described by $\dot{M} \propto r$, which is fully consistent with the hyperaccreting ADIOS model of Begelman (2012). This result is again consistent with the radial dependence of the density found in this present study.

Substituting Equations (11)–(15) into Equations (45)–(49), we can reduce the latter to the ordinary differential equations (ODEs) given in Appendix B. Equations (52)–(56) describe the variations of the five physical quantities, $v_r(\theta)$, $v_\theta(\theta)$, $v_\phi(\theta)$, $\rho(\theta)$, and $p(\theta)$ in the vertical direction.

3.2. Boundary Conditions

Following Narayan & Yi (1995), we assume that all flow variables are even symmetric, continuous, and differentiable at the equatorial plane, $\theta = \pi/2$, and the rotation axis, $\theta = 0$. The main difference here from previous works is that we include the latitudinal component of the velocity, v_θ , in our equations and consider it to be zero at both the equatorial plane and the rotation axis. Therefore, we apply the following boundary conditions at $\theta = \pi/2$ and $\theta = 0$:

$$v_\theta = \frac{d\rho}{d\theta} = \frac{dp}{d\theta} = \frac{dv_r}{d\theta} = \frac{d\Omega}{d\theta} = 0. \quad (16)$$

To solve the set of ODEs (see Equations (52)–(56) in Appendix B), we need to set the fiducial radial distance, r_0 , and the density there, ρ_0 , which are defined in Equations (11)–(15) (see the constant term, $\tau^{-1}(c/v_0)$, on the right of Equation (56) as well). Numerical simulations of accretion flow show that the radial velocity increases inward very rapidly because of the strong gravity near the black hole (Ohsuga et al. 2005; Yuan et al. 2012a, 2012b). To avoid a shock being caused supersonic inflow near the central region, which is a source of deviation from the self-similar assumptions, we neglect the region within $10r_s$, where $r_s = 2GM/c^2$ is the Schwarzschild radius (see, e.g., Kawashima et al. 2012; Jiang et al. 2014). Due to the assumption of a high mass accretion rate, we expect that strong radiation produced in the innermost region interacts with gas particles in the region $r \gtrsim 10r_s$ and strong outflow is driven there. To show the two-dimensional inflow–outflow structure of the flow, we consider all components of the velocity including v_θ in our equations. Throughout the present study, we set the inner and outer radial limits of the domain as $r_{\text{min}} = 10r_s$ and $r_{\text{max}} = 500r_s$, respectively. Thus, the assumption of a Newtonian potential is safely valid in this range. We set $r_0 = 10r_s$, and for the initial density, ρ_0 , we calculate the mass inflow rate at the outer radial boundary. Following numerical simulations of supercritical accretion flow, the dimensionless mass inflow rate

⁴ In future studies we relax this assumption and work in a regime where gas pressure and radiation pressure are comparable.

⁵ Note that Kitaki et al. (2018) showed some deviations from the self-similar assumptions.

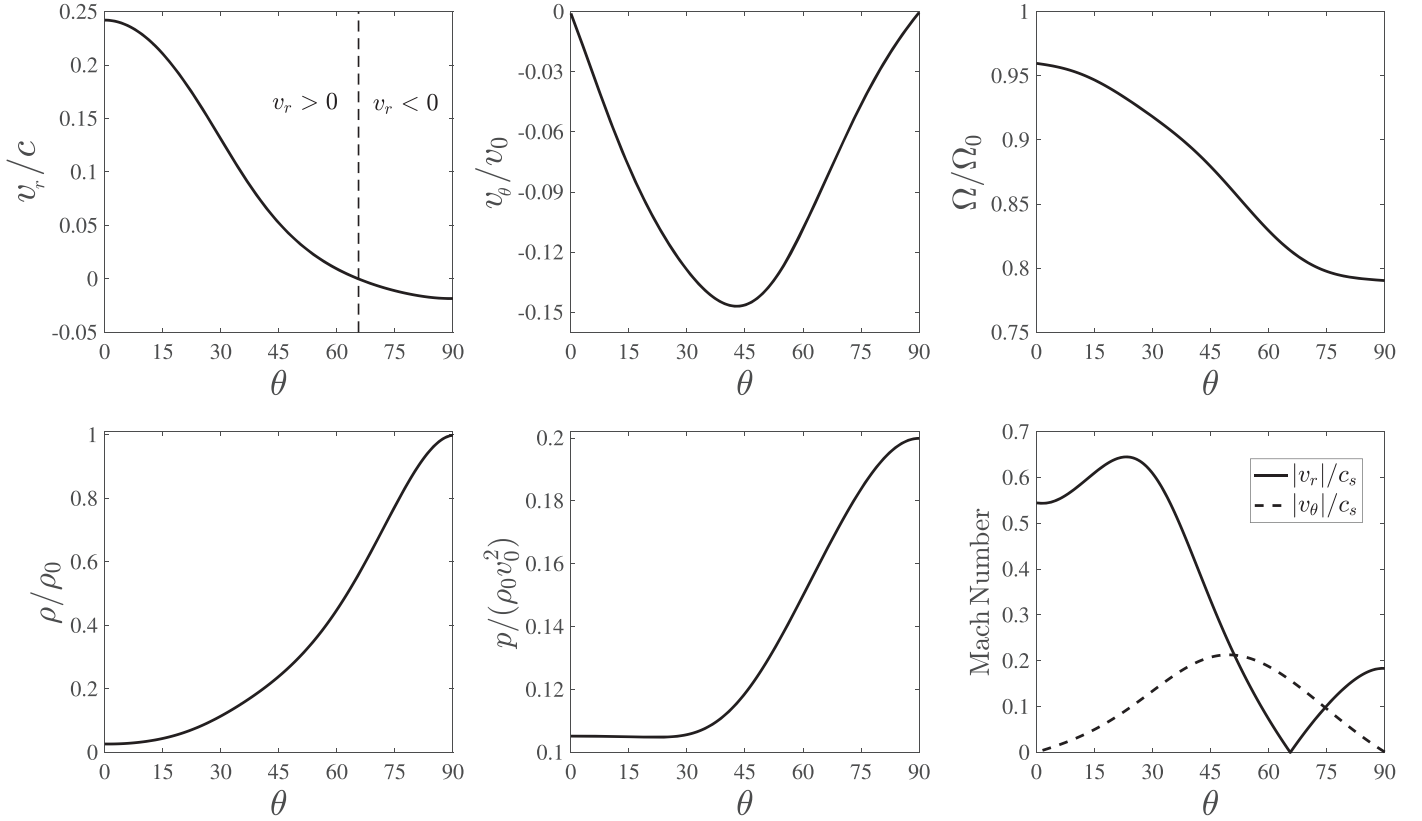


Figure 1. Angular profile of the physical variables at $r = 10r_s$. Top left panel: radial velocity in units of the light speed, c . The dashed line shows the location of $v_r = 0$, which is about 65° . Top middle panel: latitudinal velocity in units of the Keplerian velocity, v_0 . Top right panel: angular velocity in units of the Keplerian angular velocity, Ω_0 . Bottom left panel: density in units of the density of the midplane at r_0 , i.e., ρ_0 . Bottom middle panel: radiation pressure in units of $\rho_0 v_0^2$. Bottom right panel: Mach numbers.

is defined as (see Ohsuga et al. 2005; Yang et al. 2014)

$$\dot{m} = -\frac{c^2}{L_{\text{Edd}}} \int_0^\pi 2\pi r^2 \rho \min(v_r, 0) \sin \theta d\theta. \quad (17)$$

We set $\dot{m} = 1300$ at the outer radial boundary, i.e., $r_{\text{max}} = 500r_s$, throughout this paper. Based on self-similar solutions adopted here, the mass inflow rate in this study is not radially constant and decreases inward as $\dot{m} \propto r$. We use an iterative method to find the value of ρ_0 by solving Equation (17) at the outer radial boundary.

4. Numerical Results

We solve the ODEs (52)–(56) by integrating from the equatorial plane ($\theta = \pi/2$) to the rotation axis ($\theta = 0$). We adopt the values of $\alpha = 0.1$, $M = 10 M_\odot$, and $\kappa_{\text{es}} = 0.34$ with reference to the numerical simulations of Ohsuga et al. (2005) and Yang et al. (2014). The main difference here from those numerical simulations is that we consider all components of the viscous stress tensor. As stated in the previous section, the radial range of our calculation is $10r_s \leq r \leq 500r_s$. We implement a relaxation method to solve the set of equations in the vertical direction. The grid in the θ direction is divided into 2000 equally spaced points and an iterative technique is used to find the value of ρ_0 with $\dot{m} = 1300$ at r_{max} . For this constant mass accretion rate, we obtain $\rho_0 = 2.89 \times 10^{-5} \text{ g cm}^{-3}$. We can reasonably treat this value as a boundary condition. The global properties of the solutions we obtain in this way agree well with those presented in numerical simulations of Ohsuga et al. (2005) and

Yang et al. (2014). In the following subsections, we explain in detail the flow properties based upon our solutions.

4.1. Inflow–Outflow Structure of the Solutions

Figure 1 presents angular profiles of physical quantities at $r = 10r_s$. We can see that the density and the radiation pressure decrease rapidly from the equatorial plane to the rotation axis. Since we are interested in studying the case where the radiation pressure is much greater than the gas pressure, i.e., $p_{\text{gas}}/p_{\text{rad}} \ll 1$, this pressure represents the total pressure of the flow. As shown in the top left panel of Figure 1, in the region close to the equatorial plane, $\theta > 65^\circ$, the radial velocity is negative and the gas particles move toward the central black hole. In the region $\theta < 65^\circ$, the sign of the radial velocity changes and becomes positive. Furthermore, the top middle panel shows the variation of v_θ in the vertical direction. From this plot, it is seen that v_θ has a negative value at all angles, and is zero at both the equatorial plane and the rotation axis due to the boundary conditions. The minimum value of v_θ is also located around $\theta \sim 43^\circ$. Moreover, the bottom right panel of Figure 1 presents the Mach numbers. We plot this figure to check the existence of the sonic point in the high-latitude region. As we can see, no sonic points exist in this region. The Mach number $|v_r|/c_s$ decreases from the equatorial plane to about 65° , where the radial velocity is zero. Then, it increases until $\theta = 30^\circ$ and again decreases rapidly to the rotation axis. This behavior can be explained by the isothermal sound speed, $c_s = p/\rho$. The profiles of the density and the total pressure in Figure 1 show that the density decreases rapidly from the equator to the pole while the pressure is almost constant in the

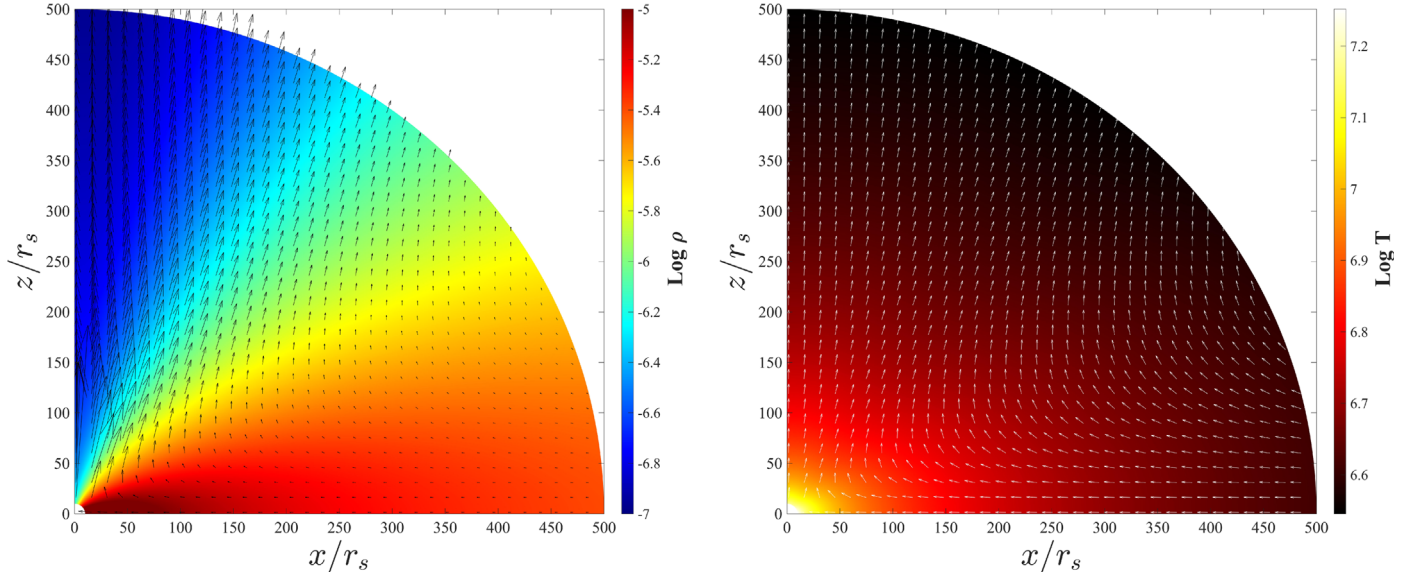


Figure 2. Two-dimensional distribution of the density (left) and the temperature (right) based on the self-similar solutions. Both panels are overlaid with the poloidal velocity. In the left panel, the poloidal velocity is normalized by $0.1c$ to denote the strength of the outflow, while in the right panel it is normalized by its absolute value to denote the direction of the vectors.

range $0 < \theta < 30^\circ$. Therefore, the Mach number declines in this range. Also, $|v_\theta|/c_s$ has a maximum value at $\theta = 43^\circ$ and becomes null at both axes due to the boundary conditions there, i.e., $v_\theta = 0$. For both lines, the Mach numbers are less than unity, which clearly shows that there is no critical point at high latitudes.

In the left panel of Figure 2, we plot the two-dimensional distribution of the density overlaid with the streamlines of the flow. The results are shown for $\dot{m} = 1300$ and the poloidal velocity is normalized by $0.1c$. It can be seen that the density tends to be larger around the midplane than around the polar axis. Moreover, the streamlines are directed toward the black hole at low latitudes with small magnitudes. At high latitudes, they are pointed outward and become outflow. For a high accretion rate, as in our present study, the outflow can be driven by the radiation pressure produced at inner radii. This strong radiation interacts with the gas particles and can push them away as a high-velocity outflow. This figure clearly shows the region of a high velocity field at high latitudes at $r = 10r_s$. As shown in the top left and top middle panels of Figure 1, the poloidal velocity of the outflow reaches about $\sim 0.25c$. These results are fully consistent with the results obtained in Yang et al. (2014, see their Figure 1) and Ohsuga et al. (2005), where the inflow is presented at low latitudes around the equatorial plane of the disk while the outflow is presented in the high-latitude regions.

The two-dimensional profile of the radiation temperature, $T = (E/a)^{1/4}$, is plotted in the right panel of Figure 2 (where $a = 7.5646 \times 10^{-15} \text{ erg cm}^{-3} \text{ K}^{-4}$ is the radiation constant). The logarithm of the temperature is overlaid with the poloidal velocity normalized by its absolute value to denote the direction of the vectors. With the assumption $p_{\text{gas}}/p_{\text{rad}} \ll 1$, the gas and the radiation are in equilibrium, so their temperatures are almost equal. Due to the heating of the gas by viscous dissipation, the temperature is higher in the inner region than at the outer radii. Therefore, this produced energy can be effectively converted into radiation energy. This figure somehow represents the distribution of the radiation internal energy density. In addition, at large radii, we can see that the temperature is lower at high

latitudes than at low latitudes. This is a consequence of radiative cooling by the outflow.

4.2. Physical Properties of the Outflow

In this subsection we calculate the physical properties of the outflow based on our self-similar solutions. The angular velocity of the accretion flow is plotted in the top right panel of Figure 1. It is seen that it increases from the equatorial plane to the rotation axis and becomes almost Keplerian at high latitudes, which is consistent with the results of numerical simulations by Yuan et al. (2012a). This indicates that the outflow can transport angular momentum outward from the disk. To check this issue in more detail, we evaluate the mass flux-weighted value of the inflow and the outflow quantities as

$$Q_{\text{in}}(r) = \frac{4\pi r^2 \int_0^{\pi/2} \rho Q \min(v_r, 0) \sin \theta d\theta}{4\pi r^2 \int_0^{\pi/2} \rho \min(v_r, 0) \sin \theta d\theta}, \quad (18)$$

$$Q_{\text{out}}(r) = \frac{4\pi r^2 \int_0^{\pi/2} \rho Q \max(v_r, 0) \sin \theta d\theta}{4\pi r^2 \int_0^{\pi/2} \rho \max(v_r, 0) \sin \theta d\theta}, \quad (19)$$

where Q represents the physical quantities. The mass flux-weighted angular momenta of the inflow and the outflow are found as

$$L_{\text{in}} = 0.79 L_K, \quad (20)$$

and

$$L_{\text{out}} = 0.89 L_K, \quad (21)$$

where L_K is the Keplerian angular momentum. This result clearly shows that the angular momentum of the flow can be transferred by the outflow, which is fully consistent with the results of numerical simulations of supercritical accretion disks (see Ohsuga et al. 2005; Yang et al. 2014). We also define the

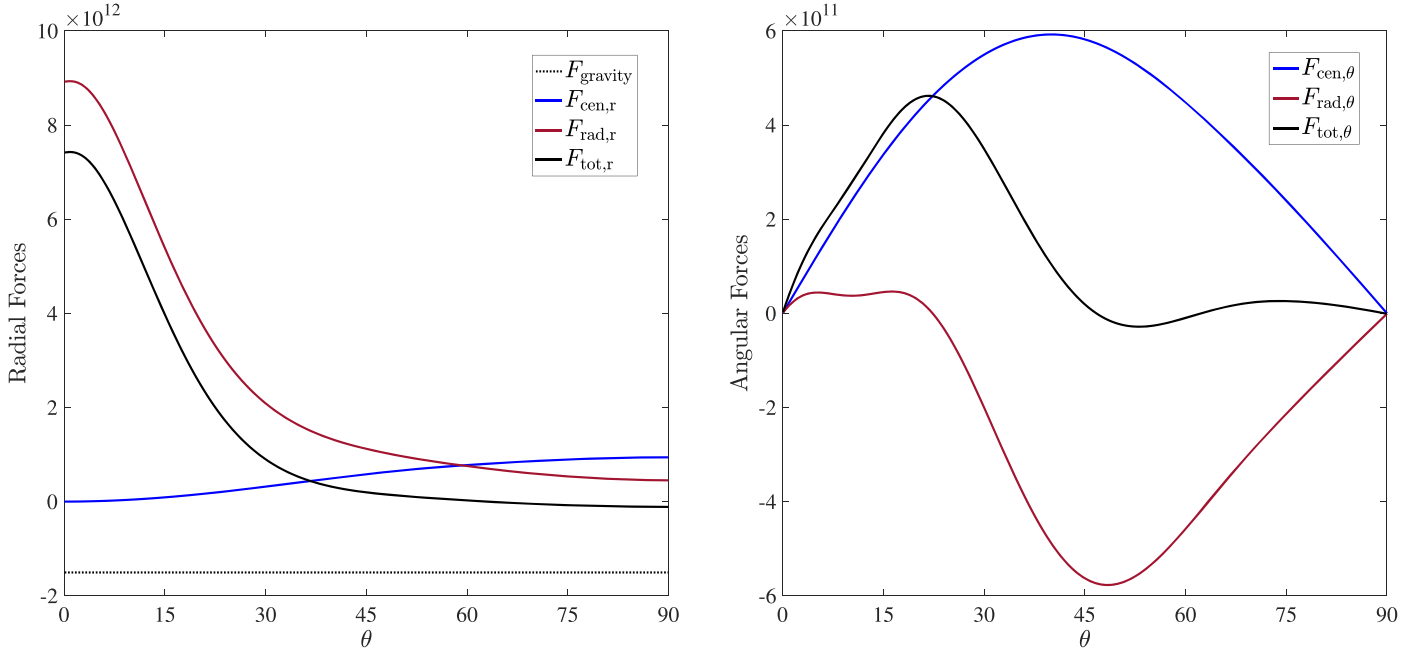


Figure 3. Angular distributions of the radial forces (left) and angular forces (right) per unit mass at $r = 10r_s$. The forces include gravity (black dotted line), centrifugal force (blue solid line), radiation force (red solid line), and their sum (black solid line).

Bernoulli parameter as

$$\text{Be}(r) = \frac{v^2}{2} + \frac{\gamma p}{(\gamma - 1)\rho} - \frac{GM}{r}, \quad (22)$$

where $\gamma = 4/3$ is the specific heat ratio. The Bernoulli parameter is the sum of the kinetic energy, the enthalpy, and the gravitational energy of the accreting gas. The mass flux-weighted Bernoulli parameter of the outflow is obtained as

$$\text{Be} = 2.67 v_K^2. \quad (23)$$

The value of the Bernoulli parameter is positive, which shows that the outflow has enough energy to overcome the gravity of the central black hole and escape to infinity. The mass flux-weighted poloidal velocity of the outflow, i.e., $v_{\text{pol}}^2 = v_r^2 + v_\theta^2$, is also calculated as

$$v_{\text{pol}} = 0.44 v_K. \quad (24)$$

Here, we conclude that the radiation-driven outflow has enough energy and power to interact with its surroundings, overcome the gravitational potential, and escape to infinity.

4.3. Analysis of Forces Driving the Outflow

In order to understand which force can drive outflow from our system, we plot in Figure 3 the angular distributions of the radial forces (left panel) and the angular forces (right panel) at $r = 10r_s$. We can see from the left panel that the angular profile of the total force has similar behavior to the angular profile of the radial velocity shown in Figure 1. In addition, the left panel of Figure 3 shows that within $60^\circ < \theta < 90^\circ$ the radial component of the centrifugal force is greater than the radial component of the radiation force and can effectively counteract the gravitational force in this range. However, within $0^\circ < \theta < 60^\circ$, the radial component of the centrifugal force decreases rapidly and becomes null at the rotation axis. In contrast, the radial component of the radiation force is the dominant force near the rotation axis, and we can see that a very strong outflow exists

near this axis. Therefore, it can be concluded that the radial radiation force is the dominant force and plays the important role of driving outflow at high latitudes. It is interesting here to compare this result with the case of hot accretion flows (Yuan et al. 2015), in which radiation can be neglected. Although the dominant driving force is different in the two cases, outflow is always present and even their properties are similar.

It is seen from the left panel of Figure 3 that the angular component of the total force is very small in the region near the equatorial plane, i.e., $50^\circ < \theta < 90^\circ$, which clearly shows that the flows are in force equilibrium in the inflow region. This is mainly because from this panel we can see that the centrifugal force balances the radiation force in the vertical direction. The angular distribution of both the radiation force and the centrifugal force become zero at both axes due to the boundary conditions.

To have a better understanding of the magnitude of the forces at different θ angles and to study the driving mechanisms of the outflow, we calculate the forces in different regions. Figure 4 shows the result at $r = 25r_s$ in the unit of gravitational force. We can see from this figure that in the inflow region, $\theta = 85^\circ$, the dominant force is gravity, so the flow moves toward the central black hole. In the intermediate region, $\theta = 45^\circ$, the driving forces are the centrifugal and radiation forces. It is seen that these forces have comparable strength, which means that both of them can drive outflow in this region, but not as strongly. Instead, at very high latitudes, $\theta = 15^\circ$, the radiation force can efficiently offset the gravity and play a noticeable role in driving the outflow, whereas the centrifugal force is negligible and does not make any effective contribution to the total force. These results are again fully consistent with those found in Yang et al. (2014) and Ohsuga et al. (2005).

4.4. Convective Stability

In terms of supercritical accretion flow, due to the large scattering optical depth, the photons produced from the innermost part of the disk are trapped and cannot efficiently escape from the

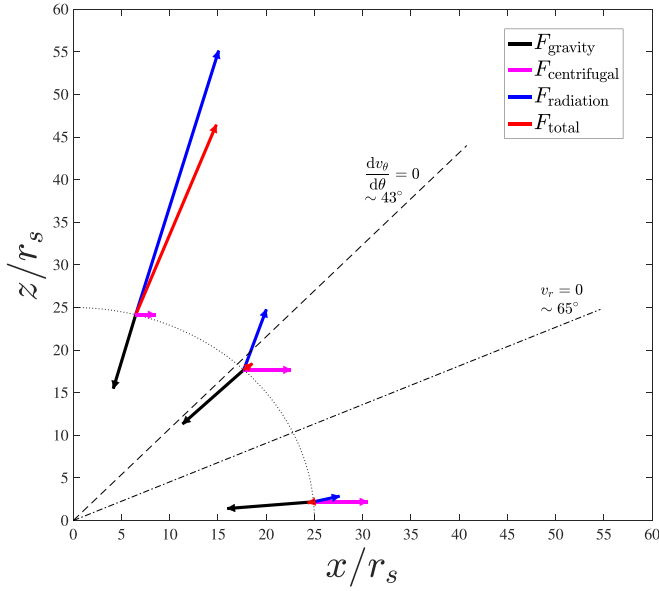


Figure 4. Force analysis in the inflow/outflow region to show the driving mechanism of the outflow at $r = 25r_s$. The length of the arrows schematically denotes the magnitude of the forces while their direction is that of the forces. The forces include gravity, centrifugal, radiation, and their sum. The dashed-dotted line shows the location of $v_r = 0$, the dashed line represents the location of $\frac{dv_\theta}{d\theta} = 0$, and the dotted line shows the radius where the forces are calculated.

disk. Furthermore, the specific entropy is dominated mostly by the radiation photons since the radiation pressure is much more important than the gas pressure here. Several analytical and simulation works have been done to study the convective stability of supercritical accretion flows. For instance, based on the local energy balance, Sadowski et al. (2009, 2011) found that the disk is convectively unstable. However, Gu (2012) used self-similar solutions and concluded that a radiation pressure-supported disk is always convectively stable. The discrepancy between these works might be related to their different definitions of the vertical structure of the disk. In terms of numerical simulation, Yang et al. (2014) studied this issue based on their simulation data for large and small values of viscosity parameter. They found that for large value of viscosity parameter, $\alpha = 0.1$, about half of the computational domain was convectively unstable, while for $\alpha = 0.005$ the unstable region was a much smaller fraction. They concluded that radiation plays an effective role in stabilizing the convection and can directly transport energy.

In this subsection, we revisit this problem and analyze the convective stability of supercritical accretion flow, in the absence of a magnetic field, based on our self-similar solutions. Thus, we use the well-known Solberg–Høiland criteria in cylindrical coordinates (R, ϕ, z) as follows:

$$\frac{1}{R^3} \frac{\partial l^2}{\partial R} - \frac{1}{C_P \rho} \nabla P \cdot \nabla S > 0, \quad (25)$$

$$-\frac{\partial P}{\partial z} \left(\frac{\partial l^2}{\partial R} \frac{\partial S}{\partial z} - \frac{\partial l^2}{\partial z} \frac{\partial S}{\partial R} \right) > 0, \quad (26)$$

where $l = r \sin \theta v_\phi$ is the specific angular momentum per unit mass, C_P is the specific heat at constant pressure, P is the total pressure, and S is the entropy defined by

$$dS \propto d \ln \left(\frac{P}{\rho^\gamma} \right). \quad (27)$$

As we stated in the previous section, we ignored the gas pressure in this study; therefore the total pressure is equal to the radiation pressure, i.e., $P = E/3$. The first Solberg–Høiland criterion can be simplified as

$$N_{\text{eff}} = \kappa^2 + N_R^2 + N_z^2 > 0, \quad (28)$$

with

$$\kappa^2 = \frac{1}{R^3} \frac{\partial l^2}{\partial R}, \quad (29)$$

$$N_R^2 = -\frac{1}{\gamma \rho} \frac{\partial P}{\partial R} \frac{\partial}{\partial R} \ln \left(\frac{P}{\rho^\gamma} \right), \quad (30)$$

$$N_z^2 = -\frac{1}{\gamma \rho} \frac{\partial P}{\partial z} \frac{\partial}{\partial z} \ln \left(\frac{P}{\rho^\gamma} \right). \quad (31)$$

Here, N_{eff} is the effective frequency, κ is the epicyclic frequency, and N_R^2 and N_z^2 are defined as the R and z components of the Brunt–Väisälä frequency, respectively. Based on our self-similar solutions, $\partial P / \partial z$ is always negative. Therefore, the second Solberg–Høiland criterion can be reduced as

$$\Delta_{IS} \equiv \frac{\partial l^2}{\partial R} \frac{\partial}{\partial z} \ln \left(\frac{P}{\rho^\gamma} \right) - \frac{\partial l^2}{\partial z} \frac{\partial}{\partial R} \ln \left(\frac{P}{\rho^\gamma} \right) > 0. \quad (32)$$

To find the angular dependence of the two Solberg–Høiland criteria in spherical coordinates, we apply the following transformations:

$$\frac{\partial}{\partial R} = \sin \theta \frac{\partial}{\partial r} + \frac{\cos \theta}{r} \frac{\partial}{\partial \theta} \quad (33)$$

$$\frac{\partial}{\partial z} = \cos \theta \frac{\partial}{\partial r} - \frac{\sin \theta}{r} \frac{\partial}{\partial \theta}. \quad (34)$$

The results are shown in Figure 5. In this figure we plot the angular variations of κ^2 , N_R^2 , N_z^2 , N_{eff}^2 normalized by Ω_K^2 , and also Δ_{IS} normalized by v_K^2 . We can see that N_R^2 is always negative, N_z^2 is very small and near zero, while κ^2 is large and positive. Consequently, N_{eff}^2 mostly follows a κ^2 pattern and is positive at all θ angles. It is seen that Δ_{IS} is negative based on our calculation. Since both Solberg–Høiland criteria are not satisfied here, we conclude that the disk is convectively unstable. This result is then valid in the absence of a magnetic field since numerical MHD simulations of accretion flow reveal that most of it is convectively stable (Narayan et al. 2012; Yuan et al. 2012a).

4.5. Energy Advection

To study the energetics of the supercritical accretion flow, we define the vertically averaged advection parameter, f_{adv} , as follows:

$$f_{\text{adv}} \equiv \frac{Q_{\text{adv}}}{Q_{\text{vis}}} = 1 - \frac{Q_{\text{rad}}^-}{Q_{\text{vis}}}, \quad (35)$$

where Q_{adv} is the energy advection rate, Q_{vis} is the viscous dissipative heating rate, and Q_{rad}^- is the radiative cooling rate. Based on our numerical results, the radiative cooling rate becomes larger than the viscous dissipation rate at high latitudes. Therefore, f_{adv} becomes negative and plays a heating role rather than a cooling one. To calculate the advection

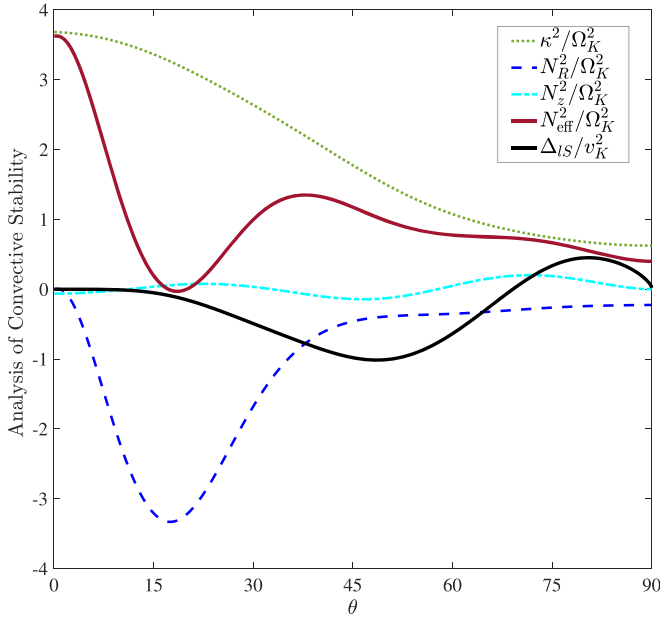


Figure 5. Angular variations of κ^2 (green dotted line), N_R^2 (blue dashed line), N_z^2 (cyan dashed-dotted line), N_{eff}^2 (red solid line), and Δ_{IS} (black solid line). The quantities κ^2 , N_R^2 , N_z^2 , and N_{eff}^2 are normalized by Ω_K^2 , and Δ_{IS} is normalized by v_K^2 .

parameter, we average this quantity over angles $\theta \geq 80^\circ$ at $r = 10r_s$ (very close to the equator). In this range the advection parameter is positive in our self-similar solution. The vertical average of the cooling/heating rates can be written as

$$Q_{\text{adv}} = 2 \int_{80^\circ}^{90^\circ} q_{\text{adv}} r \sin \theta d\theta, \quad (36)$$

$$Q_{\text{vis}} = 2 \int_{80^\circ}^{90^\circ} \Phi_{\text{vis}} r \sin \theta d\theta, \quad (37)$$

$$Q_{\text{rad}}^- = 2 \int_{80^\circ}^{90^\circ} \nabla \cdot \mathcal{F} r \sin \theta d\theta, \quad (38)$$

where q_{adv} and Φ_{vis} are the terms presented in Equation (56). We found that $f_{\text{adv}} \sim 0.62$, which is also consistent with the numerical results presented in Yang et al. (2014).

5. Summary and Discussion

We solved two-dimensional RHD equations of supercritical accretion flows in spherical coordinates and in the full r - θ space. Our calculations start from the rotation axis and work toward the equatorial plane. We adopted the Newtonian potential for the central black hole. We considered three components of the velocity and used the α prescription of the viscosity. We supposed the radiation pressure to be much greater than the gas pressure, i.e., $p_{\text{gas}}/p_{\text{rad}} \ll 1$. Consequently, the gas pressure and also the internal energy density of the gas were neglected in our calculations. By adopting self-similar solutions, we solved the ODEs as a two-point value problem and obtained the variations of the physical quantities, $v_r(\theta)$, $v_\theta(\theta)$, $v_\phi(\theta)$, $\rho(\theta)$, and $p(\theta)$ in the vertical direction. We found an inflow-outflow solution. Similar to our previous work (Zeraatgari et al. 2016), we found that the density profile can be described by $\rho(r) \propto r^{-0.5}$. Correspondingly, the radial profile of the mass inflow rate decreases with decreasing radii as $\dot{M}_{\text{in}} \propto r$. This result is fully consistent with recent analytical and numerical predictions of accretion disks (e.g., Ohsuga et al. 2005; Begelman 2012;

Yuan et al. 2012a, 2012b, 2015; Mosallanezhad et al. 2016, 2019). Our results showed that the radiation pressure and the density drop from the equatorial plane to the rotation axis. Inflow exists in the region $\theta > 65^\circ$, and above that flow moves outward and wind would launch. Our results also show that there is no sonic point above the disk. In the supercritical case, which we studied here, the radiation could push the gas particles outward and launch the wind with a poloidal velocity $\sim 0.25c$. These results are consistent with previous simulations of Yang et al. (2014) and Ohsuga et al. (2005). From our results, the temperature would drop in the wind region, and this clearly shows that the wind produced by the radiation can effectively cool the gas. By our calculations, the mass flux-weighted angular momentum of the inflow is lower than that of the wind, so the angular momentum of the flow can be transported by the wind. This result is again consistent with previous numerical simulations. One of our purposes here is to study which force can produce wind in supercritical flow. Our results show the radial component of the radiation force is the prominent force to drive outflow. We approximated the convective instability in this study. We found, unlike previous analytical works, that two Solberg-Høiland criteria were not satisfied here, so the disk is convectively unstable in the absence of the magnetic field.

There are some caveats in this work but we postpone them to our future studies. One is that we assume that the gas pressure is much lower than the radiation pressure, which is not physical. In principle, the gas and radiation pressures should be comparable to each other. Another caveat here is that the total opacity should include both absorption and scattering opacities. To avoid complexity, we neglected free-free absorption and bound-free absorption in the present study. Moreover, in accretion disk models, the magnetic field would be important in transferring angular momentum outward. In fact, the inclusion of a magnetic field will enhance the outflow as well. Therefore, in terms of a supercritical disk, it would be interesting to investigate the flow structure by combining both the radiation and the magnetic field.

We thank Feng Yuan for his thoughtful and constructive comments. Amin Mosallanezhad is supported by the Chinese Academy of Sciences President's International Fellowship Initiative (PIFI), grant No. 2018PM0046. This work is supported by the National Natural Science Foundation of China (grant No. 11725312, 11421303), the Science Challenge Project of China (grant No. TZ2016002), and the China Postdoctoral Science Foundation (grant No. 2019M663665).

Appendix A Steady-state and Axisymmetric Equations in Spherical Polar Coordinates

To simplify Equations (1)–(4), we work in spherical coordinates, (r, θ, ϕ) . We assume axisymmetric, $\partial/\partial\phi$, and steady-state, $\partial/\partial t$, flow and consider all three components of the velocity as v_r, v_θ, v_ϕ . We further assume that the accretion disk is radiation-supported, i.e., the gas pressure is negligible compared to the radiation pressure, i.e., $p_{\text{gas}}/p_{\text{rad}} \ll 1$. Therefore, the gas pressure and the internal energy density of the gas are dropped in our equations. Following Mihalas & Mihalas (1984), the components of the viscous stress tensor in spherical

coordinates are given by

$$\sigma_{rr} = 2\mu \left(\frac{\partial v_r}{\partial r} \right) - \frac{2}{3} \mu \left[\frac{1}{r^2} \frac{\partial}{\partial r} (r^2 v_r) + \frac{1}{r \sin \theta} \frac{\partial}{\partial \theta} (v_\theta \sin \theta) \right] \quad (39)$$

$$\sigma_{\theta\theta} = 2\mu \left(\frac{v_r}{r} + \frac{1}{r} \frac{\partial v_\theta}{\partial \theta} \right) - \frac{2}{3} \mu \left[\frac{1}{r^2} \frac{\partial}{\partial r} (r^2 v_r) + \frac{1}{r \sin \theta} \frac{\partial}{\partial \theta} (v_\theta \sin \theta) \right] \quad (40)$$

$$\sigma_{\phi\phi} = 2\mu \left(\frac{v_r}{r} + \frac{v_\theta \cot \theta}{r} \right) - \frac{2}{3} \mu \left[\frac{1}{r^2} \frac{\partial}{\partial r} (r^2 v_r) + \frac{1}{r \sin \theta} \frac{\partial}{\partial \theta} (v_\theta \sin \theta) \right] \quad (41)$$

$$\sigma_{r\theta} = \sigma_{\theta r} = \mu \left[\frac{1}{r} \frac{\partial v_r}{\partial \theta} + r \frac{\partial}{\partial r} \left(\frac{v_\theta}{r} \right) \right] \quad (42)$$

$$\sigma_{r\phi} = \sigma_{\phi r} = \mu r \frac{\partial}{\partial r} \left(\frac{v_\phi}{r} \right) \quad (43)$$

$$\sigma_{\theta\phi} = \sigma_{\phi\theta} = \mu \left[\frac{\sin \theta}{r} \frac{\partial}{\partial \theta} \left(\frac{v_\phi}{\sin \theta} \right) \right]. \quad (44)$$

By substituting the above equations and considering the assumptions described in Section 2, the basic equations take the form

$$\frac{1}{r^2} \frac{\partial}{\partial r} (r^2 \rho v_r) + \frac{1}{r \sin \theta} \frac{\partial}{\partial \theta} (\sin \theta \rho v_\theta) = 0, \quad (45)$$

$$\begin{aligned} \rho \left[v_r \frac{\partial v_r}{\partial r} + \frac{v_\theta}{r} \left(\frac{\partial v_r}{\partial \theta} - v_\theta \right) - \frac{v_\phi^2}{r} \right] &= -\rho \frac{GM}{r^2} + \frac{\rho \kappa_{es}}{c} F_r \\ &+ \frac{\partial}{\partial r} \left\{ 2\mu \frac{\partial v_r}{\partial r} - \frac{2}{3} \mu \left[\frac{1}{r^2} \frac{\partial}{\partial r} (r^2 v_r) + \frac{1}{r \sin \theta} \frac{\partial}{\partial \theta} (v_\theta \sin \theta) \right] \right\} \\ &+ \frac{1}{r} \frac{\partial}{\partial \theta} \left\{ \mu \left[r \frac{\partial}{\partial r} \left(\frac{v_\theta}{r} \right) + \frac{1}{r} \frac{\partial v_r}{\partial \theta} \right] \right\} + \frac{\mu}{r} \left[4r \frac{\partial}{\partial r} \left(\frac{v_r}{r} \right) \right. \\ &\left. - \frac{2}{r \sin \theta} \frac{\partial}{\partial \theta} (v_\theta \sin \theta) + r \cot \theta \frac{\partial}{\partial r} \left(\frac{v_\theta}{r} \right) + \frac{\cot \theta}{r} \frac{\partial v_r}{\partial \theta} \right], \end{aligned} \quad (46)$$

$$\begin{aligned} \rho \left[v_r \frac{\partial v_\theta}{\partial r} + \frac{v_\theta}{r} \left(\frac{\partial v_\theta}{\partial \theta} + v_r \right) - \frac{v_\phi^2}{r} \cot \theta \right] &= \frac{\rho \kappa_{es}}{c} F_\theta + \frac{\partial}{\partial r} \left\{ \mu \left[r \frac{\partial}{\partial r} \left(\frac{v_\theta}{r} \right) + \frac{1}{r} \frac{\partial v_r}{\partial \theta} \right] \right\} \\ &+ \frac{1}{r} \frac{\partial}{\partial \theta} \left\{ \frac{2\mu}{r} \left(\frac{\partial v_\theta}{\partial \theta} + v_r \right) \right. \\ &\left. - \frac{2}{3} \mu \left[\frac{1}{r^2} \frac{\partial}{\partial r} (r^2 v_r) + \frac{1}{r \sin \theta} \frac{\partial}{\partial \theta} (v_\theta \sin \theta) \right] \right\} \\ &+ \frac{\mu}{r} \left\{ \frac{2 \cot \theta}{r} \left[\sin \theta \frac{\partial}{\partial \theta} \left(\frac{v_\theta}{\sin \theta} \right) \right] + 3r \frac{\partial}{\partial r} \left(\frac{v_\theta}{r} \right) + \frac{3}{r} \frac{\partial v_r}{\partial \theta} \right\}, \end{aligned} \quad (47)$$

$$\begin{aligned} \rho \left[v_r \frac{\partial v_\phi}{\partial r} + \frac{v_\theta}{r} \frac{\partial v_\phi}{\partial \theta} + \frac{v_\phi}{r} (v_r + v_\theta \cot \theta) \right] &= \frac{\partial}{\partial r} \left[\mu r \frac{\partial}{\partial r} \left(\frac{v_\phi}{r} \right) \right] + \frac{1}{r} \frac{\partial}{\partial \theta} \left[\frac{\mu \sin \theta}{r} \frac{\partial}{\partial \theta} \left(\frac{v_\phi}{\sin \theta} \right) \right] \\ &+ \frac{\mu}{r} \left[3r \frac{\partial}{\partial r} \left(\frac{v_\phi}{r} \right) + \frac{2 \cos \theta}{r} \frac{\partial}{\partial \theta} \left(\frac{v_\phi}{\sin \theta} \right) \right], \end{aligned} \quad (48)$$

$$\begin{aligned} \frac{1}{r^2} \frac{\partial}{\partial r} (r^2 E v_r) + \frac{1}{r \sin \theta} \frac{\partial}{\partial \theta} (\sin \theta E v_\theta) &+ \frac{E}{3} \left[\frac{\partial v_r}{\partial r} + \frac{1}{r} \left(\frac{\partial v_\theta}{\partial \theta} + v_r \right) + \frac{1}{r} (v_r + v_\theta \cot \theta) \right] \\ &= -\frac{1}{r^2} \frac{\partial}{\partial r} (r^2 F_r) - \frac{1}{r \sin \theta} \frac{\partial}{\partial \theta} (\sin \theta F_\theta) \\ &+ 2\mu \left\{ \left(\frac{\partial v_r}{\partial r} \right)^2 + \left(\frac{1}{r} \frac{\partial v_\theta}{\partial \theta} + \frac{v_r}{r} \right)^2 + \left(\frac{v_r}{r} + \frac{v_\theta \cot \theta}{r} \right)^2 \right. \\ &+ \frac{1}{2} \left[r \frac{\partial}{\partial r} \left(\frac{v_\theta}{r} \right) + \frac{1}{r} \frac{\partial v_r}{\partial \theta} \right]^2 + \frac{1}{2} \left[r \frac{\partial}{\partial r} \left(\frac{v_\phi}{r} \right) \right]^2 \\ &+ \frac{1}{2} \left[\frac{\sin \theta}{r} \frac{\partial}{\partial \theta} \left(\frac{v_\phi}{\sin \theta} \right) \right]^2 \left. \right\} \\ &- \frac{2}{3} \mu \left[\frac{1}{r^2} \frac{\partial}{\partial r} (r^2 v_r) + \frac{1}{r \sin \theta} \frac{\partial}{\partial \theta} (v_\theta \sin \theta) \right]^2, \end{aligned} \quad (49)$$

where

$$F_r = -\frac{c}{3\rho\kappa_{es}} \frac{\partial E}{\partial r}, \quad (50)$$

$$F_\theta = -\frac{c}{3\rho\kappa_{es}} \frac{1}{r} \frac{\partial E}{\partial \theta}. \quad (51)$$

Appendix B Ordinary Differential Equations

By applying Equations (11)–(15) to partial differential equations in Appendix A (Equations (45)–(49)), we obtain the following five coupled ODEs in the θ direction:

$$\rho \left[v_r + v_\theta \cot \theta + \frac{dv_\theta}{d\theta} \right] + v_\theta \frac{d\rho}{d\theta} = 0 \quad (52)$$

$$\begin{aligned} \rho \left[-\frac{1}{2} v_r^2 + v_\theta \frac{dv_r}{d\theta} - v_\theta^2 - \Omega^2 \sin^2 \theta \right] &= -\rho + \frac{3}{2} p + \alpha p \frac{d^2 v_r}{d\theta^2} \\ &+ \alpha \left\{ \left[-3v_r + \frac{dv_r}{d\theta} \cot \theta - \frac{5}{2} \left(\frac{dv_\theta}{d\theta} + v_\theta \cot \theta \right) \right] p \right. \\ &\left. + \left[\frac{dv_r}{d\theta} - \frac{3}{2} v_\theta \right] \frac{dp}{d\theta} \right\} \end{aligned} \quad (53)$$

$$\begin{aligned}
& \rho \left[\frac{1}{2} v_r v_\theta + v_\theta \frac{dv_\theta}{d\theta} - \cos \theta \sin \theta \Omega^2 \right] \\
& = -\frac{dp}{d\theta} + \frac{4}{3} \alpha p \frac{d^2 v_\theta}{d\theta^2} \\
& + \alpha \left\{ \left[\frac{5}{2} \frac{dv_r}{d\theta} - v_\theta \left(\frac{9}{4} + \frac{4}{3} \cot^2 \theta \right) + \frac{4}{3} \frac{dv_\theta}{d\theta} \cot \theta \right] p \right. \\
& \left. + \left[v_r + \frac{4}{3} \frac{dv_\theta}{d\theta} - \frac{2}{3} v_\theta \cot \theta \right] \frac{dp}{d\theta} \right\} \quad (54)
\end{aligned}$$

$$\begin{aligned}
& \rho \left[\frac{1}{2} v_r \Omega \sin \theta + v_\theta \frac{d\Omega}{d\theta} \sin \theta + 2 v_\theta \Omega \cos \theta \right] \\
& = \alpha \left\{ -\frac{9}{4} p \Omega \sin \theta + p \frac{d^2 \Omega}{d\theta^2} \sin \theta + \frac{dp}{d\theta} \frac{d\Omega}{d\theta} \sin \theta + 3p \frac{d\Omega}{d\theta} \cos \theta \right\} \quad (55)
\end{aligned}$$

$$\begin{aligned}
& \frac{3}{2} v_r p + 3 v_\theta \frac{dp}{d\theta} + 4p \frac{dv_\theta}{d\theta} + 4 v_\theta p \cot \theta = \tau_0^{-1} \left(\frac{c}{v_0} \right) \\
& \times \left[-\frac{1}{\rho^2} \frac{dp}{d\theta} \frac{dp}{d\theta} + \frac{1}{\rho} \frac{d^2 p}{d\theta^2} + \frac{1}{\rho} \frac{dp}{d\theta} \cot \theta \right] \\
& + \alpha p \left\{ \frac{1}{2} v_r^2 + 2 \left(v_r + \frac{dv_\theta}{d\theta} \right)^2 + 2(v_r + v_\theta \cot \theta)^2 \right. \\
& + \frac{1}{4} \left(3 v_\theta - 2 \frac{dv_r}{d\theta} \right)^2 + \sin^2 \theta \left[\frac{9}{4} \Omega^2 + \left(\frac{d\Omega}{d\theta} \right)^2 \right] \\
& \left. - \frac{2}{3} \left[\frac{3}{2} v_r + \frac{dv_\theta}{d\theta} + v_\theta \cot \theta \right]^2 \right\} \quad (56)
\end{aligned}$$

where $\tau_0 = \rho_0 r_0 \kappa_{\text{es}}$ is the midplane optical depth at r_0 . The above ODEs represent the variation of five scalar quantities, $v_r(\theta)$, $v_\theta(\theta)$, $v_\phi(\theta)$, $\rho(\theta)$, and $p(\theta)$ with θ (for simplicity, we remove the θ dependence of our physical variables in the above equations).

ORCID iDs

Fatemeh Zahra Zeraatgari  <https://orcid.org/0000-0003-3345-727X>

Amin Mosallanezhad  <https://orcid.org/0000-0002-4601-7073>

Ye-Fei Yuan  <https://orcid.org/0000-0002-7330-4756>

De-Fu Bu  <https://orcid.org/0000-0002-0427-520X>

Liquan Mei  <https://orcid.org/0000-0003-3468-8803>

References

- Abramowicz, M. A., Czerny, B., Lasota, J. P., & Szuszkiewicz, E. 1988, *ApJ*, **332**, 646
- Abramowicz, M. A., & Fragile, P. C. 2013, *LRR*, **16**, 1
- Balbus, S. A., & Hawley, J. F. 1998, *RvMP*, **70**, 1
- Begelman, M. C. 2012, *ApJ*, **749**, 3
- Begelman, M. C., & Meier, D. L. 1982, *ApJ*, **253**, 873
- Blaes, O. 2014, *SSRv*, **183**, 21
- Blandford, R. D., & Begelman, M. 1999, *MNRAS*, **303**, 1
- Blandford, R. D., & Begelman, M. 2004, *MNRAS*, **349**, 68
- Boller, T. 2000, *NewAR*, **44**, 387
- Done, C., Gierlinski, M., & Kubota, A. 2007, *A&ARv*, **15**, 1
- Eggum, G. E., Coroniti, F. V., & Katz, J. I. 1987, *ApJ*, **323**, 634
- Eggum, G. E., Coroniti, F. V., & Katz, J. I. 1988, *ApJ*, **330**, 142
- Fragile, P. C., Olejar, A., & Anninos, P. 2014, *ApJ*, **796**, 22
- Frank, J., King, A., & Raine, D. J. 2002, *Accretion Power in Astrophysics* (Cambridge: Cambridge Univ. Press)
- Fukue, J. 2004, *PASJ*, **56**, 569
- Fürst, F., Walton, D. J., Harrison, F. A., et al. 2016, *ApJL*, **831**, L14
- Gu, W. M. 2012, *ApJ*, **753**, 118
- Gu, W. M., & Lu, J. F. 2007, *ApJ*, **660**, 541
- Israel, G. L., Belfiore, A., Stella, L., et al. 2017a, *Sci*, **355**, 817
- Israel, G. L., Papitto, A., Esposito, P., et al. 2017b, *MNRAS*, **466**, L48
- Jiang, Y. F., Stone, J. M., & Davis, S. W. 2014, *ApJ*, **796**, 106
- Kaaret, P., Feng, H., & Roberts, T. P. 2017, *ARA&A*, **55**, 303
- Kato, S., Fukue, J., & Mineshige, S. 2008, *Black-Hole Accretion Disks: Towards a New Paradigm* (Kyoto: Kyoto Univ. Press)
- Kawashima, T., Ohsuga, K., Mineshige, S., et al. 2009, *PASJ*, **61**, 769
- Kawashima, T., Ohsuga, K., Mineshige, S., et al. 2012, *ApJ*, **752**, 18
- Kitaki, T., Mineshige, S., Ohsuga, K., & Kawashima, T. 2017, *PASJ*, **69**, 92
- Kitaki, T., Mineshige, S., Ohsuga, K., & Kawashima, T. 2018, *PASJ*, **70**, 108
- Koratkar, A., & Blaes, O. 1999, *PASP*, **111**, 1
- Kosec, P., Pinto, C., Walton, D. J., et al. 2018, *MNRAS*, **479**, 3978
- Levermore, C. D., & Pomraning, G. C. 1981, *ApJ*, **248**, 321
- Lynden-Bell, D., & Pringle, J. E. 1974, *MNRAS*, **168**, 37
- Makishima, K., Kubota, A., Mizuno, T., et al. 2000, *ApJ*, **535**, 632
- McClintock, J. E., Narayan, R., & Steiner, J. F. 2014, *SSRv*, **183**, 295
- McKinney, J. C., Tchekhovskoy, A., Sadowski, A., & Narayan, R. 2014, *MNRAS*, **441**, 3177
- Mihalas, D., & Mihalas, B. W. 1984, *Foundations of Radiation Hydrodynamics* (Oxford: Oxford Univ. Press)
- Miller, J. M., Fabian, A. C., & Miller, M. C. 2004, *ApJL*, **614**, L117
- Mineshige, S., Kawaguchi, T., Takeuchi, M., & Hayashida, K. 2000, *PASJ*, **52**, 499
- Mosallanezhad, A., Abbassi, S., & Beiranvand, N. 2014, *MNRAS*, **437**, 3112
- Mosallanezhad, A., Bu, D. F., & Yuan, F. 2016, *MNRAS*, **456**, 2877
- Mosallanezhad, A., Yuan, F., Ostriker, J. P., Zeraatgari, F. Z., & Bu, D.-F. 2019, *MNRAS*, **490**, 2567
- Narayan, R., Igumenshchev, I. V., & Abramowicz, M. A. 2000, *ApJ*, **539**, 798
- Narayan, R., Sadowski, A., Penna, R. F., & Kulkarni, A. K. 2012, *MNRAS*, **426**, 3241
- Narayan, R., & Yi, I. 1994, *ApJL*, **428**, L13
- Narayan, R., & Yi, I. 1995, *ApJ*, **444**, 231
- Novikov, I. D., & Thorne, K. S. 1973, in *Black Holes*, ed. C. DeWitt & B. DeWitt (New York: Gordon and Breach), 343
- Ohsuga, K., & Mineshige, S. 2007, *ApJ*, **670**, 1283
- Ohsuga, K., & Mineshige, S. 2011, *ApJ*, **736**, 2
- Ohsuga, K., Mineshige, S., Mori, M., & Kato, Y. 2009, *PASJ*, **61**, L7
- Ohsuga, K., Mori, M., Nakamoto, T., & Mineshige, S. 2005, *ApJ*, **628**, 368
- Okuda, T. 2002, *PASJ*, **54**, 253
- Okuda, T., Teresi, V., Toscano, E., & Molteni, D. 2005, *MNRAS*, **357**, 295
- Pringle, J. E. 1981, *ARA&A*, **19**, 62
- Remillard, R. A., & McClintock, J. E. 2006, *ARA&A*, **44**, 49
- Sadowski, A., Abramowicz, M., Bursa, M., et al. 2009, *A&A*, **502**, 7
- Sadowski, A., Abramowicz, M., Bursa, M., et al. 2011, *A&A*, **527**, A17
- Sadowski, A., Narayan, R., McKinney, J. C., & Tchekhovskoy, A. 2014, *MNRAS*, **439**, 503
- Sadowski, A., Narayan, R., Tchekhovskoy, A., et al. 2015, *MNRAS*, **447**, 49
- Shakura, N. I., & Sunyaev, R. A. 1973, *A&A*, **24**, 337
- Stone, J. M., Pringle, J. E., & Begelman, M. C. 1999, *MNRAS*, **310**, 1002
- Takahashi, H. R., Ohsuga, K., Kawashima, T., & Sekiguchi, Y. 2016, *ApJ*, **826**, 23
- Vierdayanti, K., Mineshige, S., & Ueda, Y. 2010, *PASJ*, **62**, 239
- Wang, J. M., & Zhou, Y. Y. 1999, *ApJ*, **516**, 420
- Watarai, K. 2006, *ApJ*, **648**, 523
- Watarai, K., & Fukue, J. 1999, *PASJ*, **51**, 725
- Watarai, K., Fukue, J., Takeuchi, M., & Mineshige, S. 2000, *PASJ*, **52**, 133
- Watarai, K., Mizuno, T., & Mineshige, S. 2001, *ApJL*, **549**, L77
- Yang, X. H., Yuan, F., Ohsuga, K., & Bu, D. 2014, *ApJ*, **780**, 79
- Yuan, F., Bu, D., & Wu, M. 2012a, *ApJ*, **761**, 130
- Yuan, F., Gan, Z. M., Narayan, R., et al. 2015, *ApJ*, **804**, 101
- Yuan, F., & Narayan, R. 2014, *ARA&A*, **52**, 529
- Yuan, F., Wu, M., & Bu, D. 2012b, *ApJ*, **761**, 129
- Zeraatgari, F. Z., & Abbassi, S. 2015, *ApJ*, **809**, 54
- Zeraatgari, F. Z., Abbassi, S., & Mosallanezhad, A. 2016, *ApJ*, **823**, 92
- Zeraatgari, F. Z., Mosallanezhad, A., Abbassi, S., & Yuan, Y. F. 2018, *ApJ*, **852**, 124